Diffusive magnetic images of upwelling patterns in the core

Peter Olson, Ikuro Sumita,[1] and Jonathan Aurnou[2]

Department of Earth and Planetary Sciences, Johns Hopkins University, Baltimore, Maryland, USA

[1]   A new technique for imaging convection in the outer core is presented, which is based on mean field electrodynamics. The method assumes a frozen magnetic flux balance for the global-scale part of the fluid velocity in the outer core and a diffusive magnetic flux balance for smaller-scale parts of the fluid velocity. The diffusive flux balance implies that local highs and lows in the magnetic field correspond approximately to fluid downwellings and upwellings, respectively. Diffusive flux produces good images of the pattern of upwellings and downwellings near the outer boundary in numerical dynamos, except near the equator. The amplitudes of the upwellings in the diffusive magnetic images correspond to the upwelling amplitudes below the Ekman boundary layer in the numerical dynamos. We have applied this technique to the Oersted initial 2000 core field model and to time-averaged models of the historical geomagnetic field on the core-mantle boundary. It indicates that high-latitude, high magnetic flux density patches correspond to downwellings in the outer core.   *INDEX TERMS:* 1507 Geomagnetism and Paleomagnetism: Core processes (8115); 1510 Geomagnetism and Paleomagnetism: Dynamo theories; 1545 Geomagnetism and Paleomagnetism: Spatial variations (all harmonics and anomalies); 1560 Geomagnetism and Paleomagnetism: Time variations—secular and long term; 1515 Geomagnetism and Paleomagnetism: Geomagnetic induction; *KEYWORDS:* Earth's core, core flow, geomagnetic secular variation, geodynamo, geodynamo models

1.   Introduction

[2]   Delineation of the fluid motions in the outer core that induce the Earth's internal magnetic field is a longstanding objective in geomagnetism. The roots of this effort can be traced back to *Halley*'s [1692] interpretation of the geomagnetic secular variation as transport of magnetic field by liquid currents flowing in channels deep in the Earth's interior. Early theories of the geodynamo [*Elsasser*, 1947; *Bullard et al.*, 1950] also interpreted secular variation as transport of magnetic field lines by core fluid motion, and they also identified other important mechanisms for modifying the magnetic field, including stretching of the field lines by the fluid and magnetic diffusion.

[3]   Since that time, most efforts to image flow in the core assume an infinitely conducting outer core fluid. The assumption of infinite electrical conduction (equivalent to zero magnetic diffusion) is the basis for the frozen flux method, in which the effects of diffusion are ignored in the magnetic induction equation. A large number of models of flow in the core based on frozen flux have been derived, for example, *Gire and Le Mouël* [1990], *Voorhies* [1986, 1995], *Whaler* [1986], *Bloxham* [1989], *Bloxham and Jackson*

[1991]. However, *Love* [1999] and *Rau et al.* [2000] have recently shown there are limitations in applying the frozen flux method to flow in the core, related to the fact that magnetic diffusion plays an essential role in the geodynamo.

[4]   Here we investigate an alternative approach to inferring core flow. Our method provides a different image of core motions, by explicitly including some of the effects of magnetic diffusion that are ignored in frozen flux. After a brief review of the frozen flux method, we derive a simple model that links the smaller-scale magnetic field structures on the core-mantle boundary to the pattern of outer core fluid upwellings, using concepts drawn from mean field electrodynamics. The method is tested against a numerical dynamo model and then applied to short time and long time average models of geomagnetic field on the northern hemisphere of the core-mantle boundary.

2.   Theory

[5]   Methods for imaging core flow using the geomagnetic field on the core-mantle boundary use some approximation of the radial component of the magnetic induction equation [*Roberts and Gubbins*, 1987]

$$\frac{\partial B_r}{\partial t} + (\mathbf{U}_h \cdot \nabla_h)B_r + B_r(\nabla_h \cdot \mathbf{U}_h) = \frac{\lambda}{r}\nabla^2(rB_r). \qquad (1)$$

The objective is to invert equation (1) for $\mathbf{U}_h$, the horizontal (tangential) component of the fluid velocity below the core-mantle boundary, given the radial component of the

---

[1]Now at the Department of Earth Sciences, Faculty of Science, Kanazawa University, Kanazawa, Japan.

[2]Now at the Department of Terrestrial Magnetism, Carnegie Institution of Washington, Washington, D. C., USA.

magnetic field B_r there and its time derivative, the secular variation $\partial B_r/\partial t$. In equation (1), λ is the magnetic diffusivity of the outer core fluid, usually assumed constant, t is time, r is the radial coordinate and the subscript h denotes spherical coordinates (θ, ϕ).

2.1. Frozen Flux Method

[6] The frozen flux method assumes the core acts like a perfectly conducting fluid, and neglects the diffusion term in equation (1). Simple scaling considerations [*Roberts and Scott*, 1965] indicate that neglecting magnetic diffusion is justified for the large-scale part of the flow in the core. The ratio of transport to diffusion terms in equation (1) is measured by the magnetic Reynolds number

$$Rm = \frac{UD}{\lambda}, \qquad (2)$$

where U and D are characteristic velocity and length scales of the fluid motion, respectively. Large magnetic Reynolds number indicates magnetic diffusion is smaller than advection. Using the outer core thickness for D and the apparent drift rate of geomagnetic field structures to define a velocity scale, equation (2) gives $Rm \simeq 300$ for the global-scale flow. Neglecting the diffusion term leads to a couple of important simplifications. First, the induction equation (1) is reduced by one order. Second, the radial derivatives of B_r are eliminated, so the tangential velocity $\mathbf{U}_h$ can be found using only B_r and its time derivative on the core-mantle boundary, both of which are fairly well known from historical geomagnetic field record [*Bloxham and Jackson*, 1992].

[7] There are several reasons, however, why frozen flux does not provide a complete picture of core flow. One reason is that the components of $\mathbf{U}_h$ represent two independent unknowns in equation (1). Some additional constraint must be placed on the flow that relates the two velocity components to each other. Various constraints have been applied in the past, motivated by dynamical arguments. Constraints that have been tried before include assuming the motion is geostrophic, steady, or toroidal. The flow patterns obtained with these different constraints are also different, as shown in the comparison by *Bloxham and Jackson* [1991].

[8] Another limitation, which all methods for inverting equation (1) suffer from, stems from the finite resolution of the geomagnetic field. Models of the geomagnetic field on the core-mantle boundary are truncated at spherical harmonic degrees around 12 or 14 [*Bloxham and Jackson*, 1992]. This appears to be an serious limitation when using the geomagnetic field to image core flow. Judging from the results of recent numerical dynamo calculations [*Christensen et al.*, 1999; *Roberts and Glatzmaier*, 2000; *Kono et al.*, 2000a], the geodynamo likely contains significant amounts of magnetic energy and kinetic energy at spherical harmonic degrees above 14. The higher-degree (i.e., smaller-scale) magnetic fields, which are closely related to the pattern of the convection in the numerical dynamos, are not resolved in the geomagnetic field on the core-mantle boundary. This is especially true for the geomagnetic secular variation.

[9] A third reason why frozen flux images of core flow are incomplete is related to the neglect of magnetic diffusion. By neglecting diffusion, the frozen flux method implies a balance between the geomagnetic secular variation and transport and stretching of the magnetic field by the fluid motion. The fluid motions imaged this way are directly proportional to the secular variation. Flows that do not induce secular variation, either because their motion is parallel to contours of the radial magnetic field [*Backus*, 1968] or because the magnetic field they induce is balanced by diffusion [*Gubbins*, 1996a, 1996b], cannot be detected this way.

[10] The frozen flux approach to imaging core flow has recently been tested using magnetic and velocity fields obtained from numerical dynamos [*Love*, 1999; *Rau et al.*, 2000; *Roberts and Glatzmaier*, 2000]. Numerical dynamo models offer the advantages that the velocity and magnetic fields are known a priori and are electromagnetically self-consistent. One simple test involves the conservation of total magnetic flux, a constraint implicit in the frozen flux approximation. *Roberts and Glatzmaier* [2000] have determined how well total magnetic flux is conserved in numerical dynamos with large but finite magnetic Reynolds number. They find that the total flux is constraint to within a few percent in their dynamo models, over timescales corresponding to a couple of hundred years in the core. A more demanding test is to compare the actual velocity pattern from the numerical dynamo with its frozen flux image, derived by applying the frozen flux method to the magnetic field from the same dynamo model. *Rau et al.* [2000] have performed this type of test on several numerical dynamos. They obtained frozen flux images of the flow using standard flow constraints, including tangentially geostrophic flow, steady flow, and toroidal flow assumptions. They report correlation coefficients of about 0.5 between the frozen flux image of the velocity and the actual velocity from the numerical dynamo. Importantly, they find that certain components of the flow are not well imaged by the frozen flux approach. In particular, *Rau et al.* [2000] find that much of the velocity field in their numerical dynamos is oriented parallel to the magnetic field contours. This component of motion does not induce secular variation of its own, and so is missing from frozen flux images.

[11] *Love* [1999] has made other tests of the frozen flux method, using nearly steady kinematic dynamos. He argues that nearly steady dynamo models constitute a good test of any imaging technique, since the core field is also nearly steady, in the sense that much of the structure in the nondipole part of the field on the core-mantle boundary evolves slowly in time. Like *Rau et al.* [2000], *Love* [1999] finds the frozen flux method fails to give the correct fluid velocity pattern, but for somewhat different reasons. *Love* [1999] concludes that the frozen flux method fails to image important components of the flow in nearly steady dynamos because it ignores diffusion. In steady state, frozen flux implies a balance between advection and stretching of magnetic field lines; in contrast, magnetic diffusion is always important in numerical dynamo models, particularly for the time-averaged field.

2.2. A Mean Field Magnetic Induction Model

[12] Some of the limitations implicit in the frozen flux approach can be overcome by distinguishing between long- and short-wavelength structures in the flow and the mag-

netic field, and including magnetic diffusion effects at short wavelengths. Distinction between long- and short-wavelengths in the fluid velocity and the magnetic field is the basis for mean field electrodynamic dynamos [see *Moffatt*, 1978; *Gubbins and Roberts*, 1987]. The assumption of separate global and local scales of magnetic field and fluid motion within the outer core is supported by the results of recent numerical dynamo models [*Glatzmaier and Roberts*, 1996; *Kuang and Bloxham*, 1997; *Kageyama and Sato*, 1997; *Christensen et al.*, 1999; *Kono et al.*, 2000a]. In these models the convection is characterized by length scales very much smaller than the core radius, and magnetic induction on these length scales involves diffusion.

[13] Here we derive the lowest-order balance of terms in the radial induction equation (1) on the surface of a fluid dynamo that involves both large- and small-scale velocity components, according to the mean field electrodynamics [*Moffatt*, 1978; *Roberts and Gubbins*, 1987]. Our derivation makes use of spatial averages rather than the time averages used by *Love* [1999]; however, our results are similar to his.

[14] We first separate the radial magnetic field and the tangential fluid velocity into large- and small-scale parts:

$$B_r = B + b \tag{3}$$

$$\mathbf{U}_h = \mathbf{U} + \mathbf{u}. \tag{4}$$

For purposes of definition, we suppose that the large-scale magnetic field and fluid velocity correspond to averages over a region of the core-mantle boundary. Denoting spatial averages by overbars gives $(\overline{B_r}, \overline{\mathbf{U}_h}) = (B, \mathbf{U})$ so that $\overline{b} = \overline{\mathbf{u}} = 0$. On scales smaller than the averaging region, the large-scale velocity and magnetic field can be considered uniform. Substituting equations (3) and (4) into (1) and averaging yields separate equations for the large-scale magnetic field

$$\frac{\partial B}{\partial t} + \overline{(\mathbf{u} \cdot \nabla_h)b} + \overline{b(\nabla_h \cdot \mathbf{u})} = \frac{\lambda}{r} \nabla^2 (rB) \tag{5}$$

and for the small-scale magnetic field

$$\frac{\partial b}{\partial t} + (\mathbf{U} \cdot \nabla_h)b + B(\nabla_h \cdot \mathbf{u}) + G = \frac{\lambda}{r} \nabla^2 (rb), \tag{6}$$

where

$$G = (\mathbf{u} \cdot \nabla_h)b - \overline{(\mathbf{u} \cdot \nabla_h)b} + b(\nabla_h \cdot \mathbf{u}) - \overline{b(\nabla_h \cdot \mathbf{u})}. \tag{7}$$

The steady state version of equation (5) corresponds to equation 11 used by *Love* [1999] and equation (6) corresponds to his equation 12.

[15] In mean field electrodynamics, it is usual to assume first-order smoothness, in which the term G is neglected in equation (6). *Moffatt* [1978] gives some examples of situations where this assumption is justified. In section 3, we show that G is, in fact, negligible compared to other terms in equation (6) for the numerical dynamos we analyze. In addition to first-order smoothness, we also assume local equilibrium. For local equilibrium, the smaller-scale magnetic field structures are steady in a frame of reference moving with the large-scale velocity $\mathbf{U}$. This is equivalent to

the following frozen flux balance between the secular variation of the small-scale field and the large-scale flow:

$$\frac{\partial b}{\partial t} + (\mathbf{U} \cdot \nabla_h)b = 0. \tag{8}$$

With these assumptions, equation (6) reduces to

$$B(\nabla_h \cdot \mathbf{u}) = \frac{\lambda}{r} \nabla^2 (rb). \tag{9}$$

[16] The final step is to properly evaluate equation (9) on the core-mantle boundary $r = R$. Here two more difficulties arise, related to the fact that both remaining terms in equation (9) vary with depth below the core-mantle boundary, and neither the magnetic field nor the fluid velocity are known inside the core. Consider first the problem of evaluating the radial derivatives in the diffusion term. Apart from the constraint that the radial component of the magnetic field is continuous at the core-mantle boundary, we have little information on how the field varies with depth inside the electrically conducting core. Since we cannot compute radial derivatives of the geomagnetic field within the core, the most expedient way to deal with the contribution from radial magnetic diffusion is to simply ignore it and keep only the tangential diffusion term in equation (9). This procedure is justifiable only in those places where tangential diffusion exceeds radial diffusion. *Gubbins* [1996] has argued that the relative importance of radial magnetic diffusion is related to the presence or absence of boundary layers in the tangential electric current. In our numerical dynamos, we find that tangential diffusion tends to dominate over radial diffusion at high magnetic latitudes, where the magnetic field lines are nearly radial. Conversely, the opposite relationship is found at low magnetic latitudes, where the field lines are more nearly tangential.

[17] The second problem with evaluating equation (9) on the core-mantle boundary is that $\nabla_h \cdot \mathbf{u}$ varies rapidly with depth. To the extent that the core mantle boundary approximates an impermeable, equipotential surface, $\nabla_h \cdot \mathbf{u} = 0$ at $r = R$ but is generally nonzero for $r < R$. It is therefore not clear what depth (or, what depth interval) the upwelling term in equation (9) actually represents. The argument that is usually given to overcome this ambiguity is that the imaged velocities correspond to fluid motion in the free stream, at some finite depth in the core, beneath the velocity boundary layers that must be present below the core-mantle boundary [*Roberts and Gubbins*, 1987]. According to this argument, the variation of the free stream velocity with depth is small and can be ignored, so that the upwelling term in equation (9) can be treated as depth-independent.

[18] This argument is perhaps justifiable for interpreting global-scale velocities in the core, but the results of numerical dynamo models give a somewhat different picture for the smaller-scale velocity field. The velocity boundary layers in numerical dynamos are typically quite thin and indeed they seem to have little influence on the global structure of the magnetic field [*Christensen et al.*, 1999; *Kono et al.*, 2000a]. However, these same dynamo models show that there is no well-defined free stream region, where the fluid velocities attain constant (depth-independent) values. Instead the amplitudes of the velocities and the upwel-

lings associated with them vary continuously with depth beneath the boundary. Accordingly, when we evaluate the first term in This argument is perhaps(9) on the surface $r = R$, we are in fact projecting the three-dimensional upwelling onto the two-dimensional outer spherical boundary.

[19] In order to emphasize this distinction, we define $w' = \overline{\nabla_h \cdot \mathbf{u}}$ to be the upwelling image, a depth-averaged projection of the three-dimensional upwelling onto the outer boundary. Then equation (9) becomes

$$Bw' = \lambda \nabla_h^2 b \qquad (10)$$

on $r = R$, with

$$\nabla_h^2 = \frac{1}{R^2 \sin\theta} \left(\frac{\partial}{\partial\theta} \sin\theta \frac{\partial}{\partial\theta} + \frac{1}{\sin\theta} \frac{\partial^2}{\partial\phi^2} \right). \qquad (11)$$

According to equation (10), tangential diffusion of small-scale magnetic field is correlated with fluid upwellings in dynamos with mean field electrodynamic effects. For this class of dynamos, and possibly more generally, tangential magnetic diffusion on the outer boundary can be used to image the convection pattern in the fluid.

[20] There is another useful result from mean field electrodynamics that has been substantiated in numerical dynamo models, which provides a way to image the non-divergent part of the tangential velocity, including the tangential velocity parallel to magnetic field contours that produces no magnetic secular variation of its own. Magnetic induction in rotating, convection-driven dynamos occurs primarily through the mean field "alpha effect" [*Moffatt*, 1978], which is proportional to the volume average helicity of the convective motions. Helicity is the inner product of fluid vorticity, $\xi = \nabla \times \mathbf{u}$, and velocity:

$$H = \xi \cdot \mathbf{u}. \qquad (12)$$

Numerical dynamo models driven by convection in rotating spherical geometry show large amounts of helicity associated with columnar convection [*Glatzmaier and Roberts*, 1996; *Kuang and Bloxham*, 1997; *Christensen et al.*, 1999]. The helicity in these dynamos is due to the combination of quasi-geostrophic flow around the convection columns and ageostrophic flow along the axis of the columns, the latter being driven by the combined effects of buoyancy and Ekman pumping. (The dissipative Ekman pumping tends to restore the flow toward the state of solid body rotation.) Convection columns with positive axial vorticity (vorticity parallel to the planetary rotation, i.e., cyclones) have axial downwellings near the outer boundary, whereas convection columns with negative axial vorticity (anticyclones) have axial upwellings [*Olson et al.*, 1999]. For these reasons, the average helicity in convection-driven dynamo models tends to be negative in the northern hemisphere and positive in the southern hemisphere. Negative helicity at high northern latitudes, for example, means that the radial component of vorticity ξ_r and the radial component of velocity u_r are negatively correlated there. Near the outer boundary, the radial velocity pattern is similar to the upwelling pattern. So the negative helicity in the northern hemisphere also means that the radial vorticity ξ_r is negatively correlated with the

fluid upwelling w' near the outer boundary. This relationship holds particularly at high latitudes.

[21] Suppose that we represent proportionality between $-\xi_r$ and w' at high latitudes near the outer boundary with a coefficient c. The radial vorticity is related to the toroidal stream function ψ via $\xi_r = -\nabla_h^2 \psi$. Then the toroidal stream function can then be calculated from the upwelling obtained from equation (10) by solving the following equation over the outer boundary:

$$\nabla_h^2 \psi = cw'. \qquad (13)$$

Note that most of the toroidal velocity $u = \nabla \times \hat{\mathbf{r}}\, \psi$ obtained from solving equation (13) lies in the null-space, that is, it is parallel to the contours of the small-scale magnetic field [*Backus*, 1968]. The relationship between small magnetic field variations b and the toroidal stream function ψ is particularly simple in regions where the large-scale field B can be considered uniform. Then equations (10) and (13) combine to give the following linear relation between the toroidal stream function and the small-scale magnetic field in that region:

$$\psi = c\left(\frac{\lambda}{B}\right) b. \qquad (14)$$

This result indicates that over those portions of the boundary where the large-scale magnetic field is approximately uniform and where the assumption of local equilibrium is met, contours of the small-scale magnetic field correspond approximately to stream lines of the toroidal fluid motion. The scale factor between the stream function and the small-scale field in equation (14) includes the magnetic diffusivity, the large-scale field intensity and the coefficient c introduced in equation (13). The value of c depends on the dynamics of the convection. In the special case that upwelling is entirely due to Ekman pumping at the outer boundary, then $c \simeq 2R/d$, where R is the core radius and $d \simeq \sqrt{\nu/\Omega}$ is the Ekman boundary layer thickness where ν is the kinematic viscosity [*Greenspan*, 1968]. In a dynamo, other forces such as buoyancy and the Lorentz force contribute to the upwelling, so the coefficient c depends on other effects in addition to the strength of Ekman pumping.

[22] In the numerical dynamo models, the magnetic induction is scaled by the Elsasser number is $\Lambda = \sigma\, B^2/\rho\Omega$. Here σ is electrical conductivity, ρ is density, and Ω is angular velocity of rotation. The Elsasser number defines the scale factor $(\rho\Omega/\sigma)^{1/2}$ for converting the dimensionless magnetic field in the numerical dynamos to dimensional units of magnetic induction. Using asterisks to indicate dimensionless variables, the dimensional and dimensionless versions of the small-scale magnetic field are related by

$$b^* = \left(\frac{\sigma}{\rho\Omega}\right)^{1/2} b. \qquad (15)$$

For comparison with the images derived from geomagnetic data, it is also useful to define nondimensional versions of the upwelling $\nabla_h \cdot \mathbf{u}$, the upwelling image w', the vorticity ξ, and the stream function ψ. Again using asterisks to denote

dimensionless variables, these are related to their dimensional counterparts by

$$(\nabla_h \cdot \mathbf{u}^*, w^*, \xi^*) = \frac{D^2}{\lambda}(\nabla_h \cdot \mathbf{u}, w', \xi) \qquad (16)$$

$$\psi^* = \frac{\psi}{\lambda}. \qquad (17)$$

The magnitude of each of these dimensionless variables is essentially the magnetic Reynolds number of that quantity. The results of our dynamo model calculations and the results of our geomagnetic field analyses are given in terms of these variables.

[23] A practical difficulty in numerically calculating a diffusive upwelling image using a magnetic field model with equation (10) stems from the singularity in the inverse of equation (10) near the magnetic equator of the large-scale field. We have tried two different solution methods to overcome this problem. In the first method we evaluate equation (10) directly for w' everywhere on the sphere, except in a band around the main field equator. We define this band is as the region where the main field is less than 2% of its global maximum value. For most dynamo models examined, this band extends about ±4° about the main field equator. We then use spline functions to interpolate the field image across the band. In the second method we solve for w' globally, using singular value decomposition with spherical harmonic basis functions. The results of these two approaches are grossly similar, although we do find some differences between them near the main field equator. Since the first method seems to produce smoother images, we show the results obtained using it. However, with both solution methods we find that the results of this method are not very robust at low magnetic latitudes. Small differences in magnetic field structure lead to large differences in the upwelling image there. Instability in the solutions in this region occurs because assumptions underlying equation (10) are generally not valid at low latitudes. In particular, the balance between radial stretching and tangential diffusion which forms the basis of equation (10) is not appropriate at low magnetic latitudes, since radial diffusion and other forms of field line stretching and transport not included in equation (10) are important there. Accordingly, although we calculate the upwelling pattern over the whole sphere, we do not interpret the images close to the equator.

3. Diffusive Flux Images of Convection in Numerical Dynamos

[24] We have tested the diffusive flux method using a number of well-resolved numerical dynamos driven by thermal convection in a rotating spherical shell. Details of the numerical dynamos, including the dimensionless parameter values, grid sizes and the structure of the flow and magnetic field they produce, are given by *Olson et al.* [1999] and *Christensen et al.* [1999]. All the dynamos calculations we have examined use the Navier-Stokes, magnetic induction, and heat equations for an incompressible Boussinesq fluid, including complete inertial terms and Newtonian viscosity. The diffusivities are constant, and no scale-dependent parameterizations such as hyperdiffu-

sivity have been used. The domain is a spherical shell with same radius ratio as the liquid outer core. The boundary conditions are simple and homogeneous: no-slip, isothermal, and electrically insulating. The numerical solution method is described by *Olson and Glatzmaier* [1996] and *Christensen et al.* [1999]. The solutions are typically time-dependent columnar convection generating a time-dependent magnetic field dominated by the axial dipole component. These dynamos are in the strong field (Elsasser number $\Lambda \simeq 1$) regime, where the Coriolis and Lorentz force have comparable magnitude.

[25] The procedure we use for constructing the upwelling image from a numerical dynamo is as follows. We run the dynamo model until the magnetic field has reached statistical equilibrium, where the power spectrum of the field has ceased to evolve, and then select a particular time snapshot of the radial component of the magnetic field on the outer boundary for analysis. The next step is to separate the radial field into a large- (global) scale and small- (local) scale parts. The definition of what constitutes the global part of the field is somewhat arbitrary in this context. For each case examined we have made parallel analyses, first using the azimuthally averaged magnetic field as the global field model, and then using the axial dipole component as the global field model. The difference between these options turns out to be minor in nearly every case. Once the definition of the global magnetic field is established, we calculate the local field according to equation (3) and solve the dimensionless version of equation (10) over the sphere for the dimensionless upwelling image w^*. We then compare this image with $\nabla_h \cdot \mathbf{u}^*$, the upwelling from the numerical dynamo model. Since the dynamo upwelling amplitude varies with depth below the outer boundary, we calculate the depth-averaged upwelling as a function of depth, from the surface $z^* = 0$ to a nominal maximum depth of $z^* = 0.1$, to determine the effective averaging depth that the diffusive image corresponds to.

[26] A typical test case is shown in Figure 1. The maps are northern hemisphere polar projections of a snapshot in time from a convective dynamo in the regime of strongly columnar flow. The dimensionless parameters of the calculation have the following values: Rayleigh number $Ra = 8 \times 10^6$ (nearly 5 times critical), Ekman number $E = 10^{-4}$, Prandtl number $Pr = 1$, magnetic Prandtl number $Pm = 2$. Here $Ra = \alpha g \Delta T D^3 / \nu \kappa$, $Ek = \nu / \Omega D^2$, $Pr = \nu / \kappa$ and $Pm = \nu / \lambda$, where α is the thermal expansion coefficient, g is gravity on the outer boundary, ΔT is the temperature difference across the spherical shell and Ω is the planetary angular velocity. The kinematic viscosity and thermal diffusivity are ν and κ, respectively. The basic length scale used in these parameters is the shell thickness $D = R_o - R_i$, where R_o and R_i are the outer and inner radii, and the basic timescale is the viscous diffusion time across the shell, D^2 / ν. The calculation was made using a finite difference grid with 33, 80, and 160 points in radius, latitude, and longitude, respectively, and truncation at spherical harmonic degree $l_{max} = 64$. Twofold azimuthal symmetry is imposed on the solution.

[27] The axisymmetric part of the magnetic field generated by this dynamo is very nearly an axial dipole. Because the flow in this dynamo is nearly symmetric and the magnetic field is nearly antisymmetric with respect to the
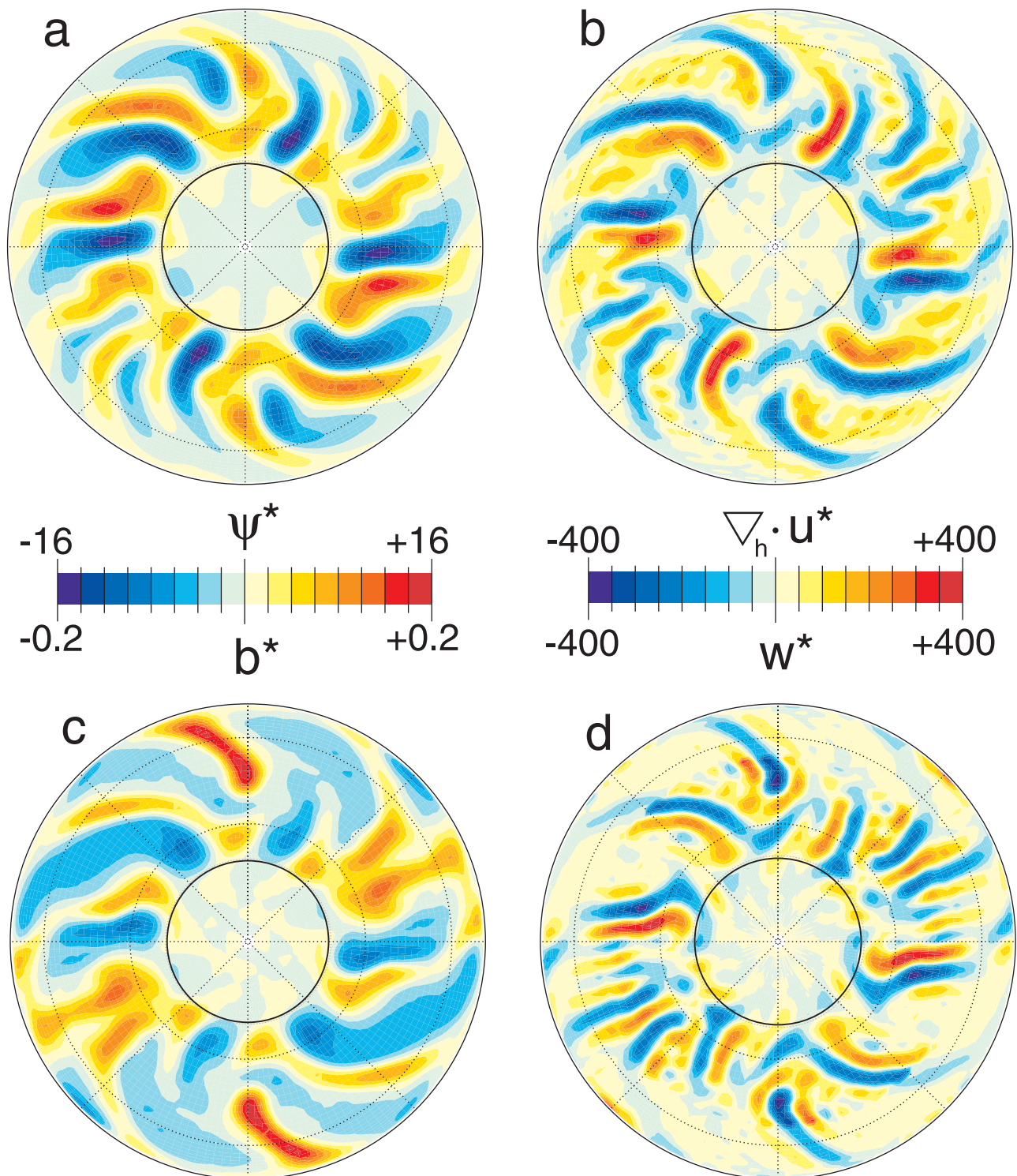
Figure 1. Comparison of upwelling planform with its diffusive magnetic image in a dynamo driven by strongly columnar-style thermal convection in a rotating spherical shell at $Ra = 8 \times 10^6 (\simeq 4.8 \times Ra_c)$, $E = 1 \times 10^{-4}$, and $Pr = 1$, $Pm = 2$. See text for other calculation parameters and scalings of the dimensionless variables. Shown are northern hemisphere projections with the outer circle representing the outer boundary equator and the inner circle representing the tangent cylinder, the axial projection of the inner spherical boundary onto the outer boundary. (a) Stream function of toroidal motion at depth $z^* = 0.07$ beneath the outer boundary (contour steps in dimensionless units defined by equation (15)). (b) Upwelling planform at depth $z^* = 0.07$ (contour steps in dimensionless units defined by equation (16)). (c) Nonaxisymmetric part of the radial magnetic field at the outer boundary $z^* = 0$ (contour steps in dimensionless units defined by equation (16)). (d) Diffusive magnetic image of upwelling (contour steps in dimensionless units defined by equation (16)).

equator, the southern hemisphere is similar to what is shown in Figure 1, except that the radial magnetic field is reversed. The particular initial conditions used to begin this calculation have created a main magnetic field with reverse polarity, that is, with positive (outward directed) radial field in the northern hemisphere.

[28] Two important dimensionless output parameters that characterize the solution are the magnetic Reynolds number Rm and the Elsasser number Λ. The volume averaged Elsasser number is near unity in Figure 1, consistent with this case being a strong field dynamo. According to the definition of Rm in equation (2), the volume averaged magnetic Reynolds number of the dynamo shown in Figure 1 is about 60. This is large enough so that the planform of the convection columns does not have a simple azimuthal periodicity but instead evolves chaotically in time. However, the flow structure remains strongly columnar at all times, and each snapshot of the flow shows a pattern of columns nearly symmetric with respect to the equatorial plane. There is a small, statistical azimuthal drift in the convection pattern, but the average azimuthal drift speed is significantly less than the characteristic speed of the fluid around the convection columns.

[29] Figure 1a shows a snapshot of ψ^*, the toroidal stream function of the fluid motion at a depth $z^* = 0.07$, just below the outer boundary Ekman layer, over the northern hemisphere of the dynamo. Figure 1b shows the upwelling pattern from the numerical dynamo at the same time, averaged over the depth interval from $z^* = 0$ to $z^* = 0.07$. Although the pattern of the upwelling changes little with depth near the outer boundary, the amplitude of the upwelling varies strongly with depth. The upwelling amplitude increases from zero at depth $z^* = 0$, a consequence of the no-slip velocity condition used at the outer boundary, reaches a maximum within the Ekman layer, and then decreases below that. Figure 1c shows the nonaxisymmetric part of the radial magnetic field over the same portion of the northern hemisphere on the outer boundary of the dynamo. Figure 1d is w^*, the diffusive magnetic image of the upwelling pattern, obtained by solving the dimensionless version of equation (10) using the nonzonal magnetic field from Figure 1a. The contour intervals used in the upwelling image (Figure 1d) are the same as in the dynamo upwelling (Figure 1b).

[30] Comparison of Figures 1b and 1d demonstrates how the diffusive magnetic image contains many of the important elements of the dynamo upwelling pattern, especially in the high-latitude zone where the columnar convection intersects the outer boundary. Nearly all of the intense, small-scale upwellings and downwellings arrayed around the inner core tangent cylinder in the dynamo are also present in the image.

[31] Figure 2 shows scatterplots between pairs of important variables from this dynamo, obtained using the values on the numerical grid at the outer surface $z^* = 0$ and at depth $z^* = 0.07$. Note that the vorticity and surface divergence are particularly well correlated in Figure 2a. The global (full sphere) correlation between the dynamo upwelling pattern and its diffusive image is about 0.89 in this case. However, there is a large variation in the correlation with latitude. In particular, Figure 1 shows that the upwellings in the image tend to be enhanced at lower latitudes, compared to the

upwellings in the dynamo model. As shown in Figure 3, the correlation often exceeds 0.9 in the latitude zone where the columns intersect the outer boundary, whereas it drops to about 0.7 closer to the equator. This latitude dependent deviation accounts for about one half of the scatter between the variables shown in Figure 2, and is typical for the dynamo models we have examined. The systematic deviation with latitude between the dynamo upwelling and its image is partly a consequence of the somewhat arbitrary distinction between the large-scale and the small-scale magnetic fields in equation (3), but more importantly it reflects the fact that approximations used to derive equation (10) become increasingly less valid at low latitudes. In contrast, the anomalously low correlation at both poles in Figure 3 is a localized artifact, due to our particular choice of the main part of the magnetic field there.

[32] For this dynamo, the RMS amplitudes of the diffusive magnetic image matches the upwelling amplitude at the depth $z^* = 0.07$, which corresponds approximately to the base of the viscous Ekman boundary layer. At this particular depth the image accounts for approximately 75% of the variance in the dynamo upwelling.

[33] Several of the key assumptions we have used can be justified, by calculating the magnitude of the terms neglected in the derivation of equation (10) from equation (1). One of our critical assumptions is first-order smoothness, used to justify neglect of the function G in equation (6). The ratio of the RMS amplitude of G is in fact nearly always small compared to the diffusion term in equation (6). In the dynamo shown in Figure 1 for example, the ratio of the two terms is -0.06. Another important assumption involves the helicity defined in equation (12), the correlation between vorticity and axial velocity (upwelling) in the columnar convection. Figure 2a demonstrates the strong negative correlation between radial vorticity and upwelling in the northern hemisphere. At the depth shown ($z^* = 0.07$), the correlation is -0.983, and it is larger still at shallower depths. A corollary of the assumption of correlated vorticity and axial velocity is that the upwelling image should be negatively correlated with the actual radial vorticity. Figure 2d shows these variables have a crude negative correlation, the coefficient being -0.82 in this case.

[34] Finally, Figures 1 and 2 demonstrate that the perturbation magnetic field contours indeed do approximate the streamlines of the toroidal motion, as predicted by equation (14). Figure 1a shows the stream function of the toroidal motion ψ below the outer boundary Ekman layer. Comparison with Figure 1c shows the similarity between the stream function and the nonaxisymmetric radial field structure: nonaxisymmetric field highs mark positive (cyclonic) vortices and nonaxisymmetric field lows mark negative (anticyclonic) vortices. Although there is significant scatter in this relationship (in particular, high field values do not fit well for the reason given above), the global correlation is still large, about $+ 0.9$. This is another demonstration that in dynamos driven by columnar-style convection, much of the fluid circulation is along magnetic field contours, consistent with the findings of *Rau et al.* [2000].

[35] The observed similarity between ψ^* and b^* supports the local equilibrium assumption used to derive equation (10). It also provides a way to estimate the inert part of the
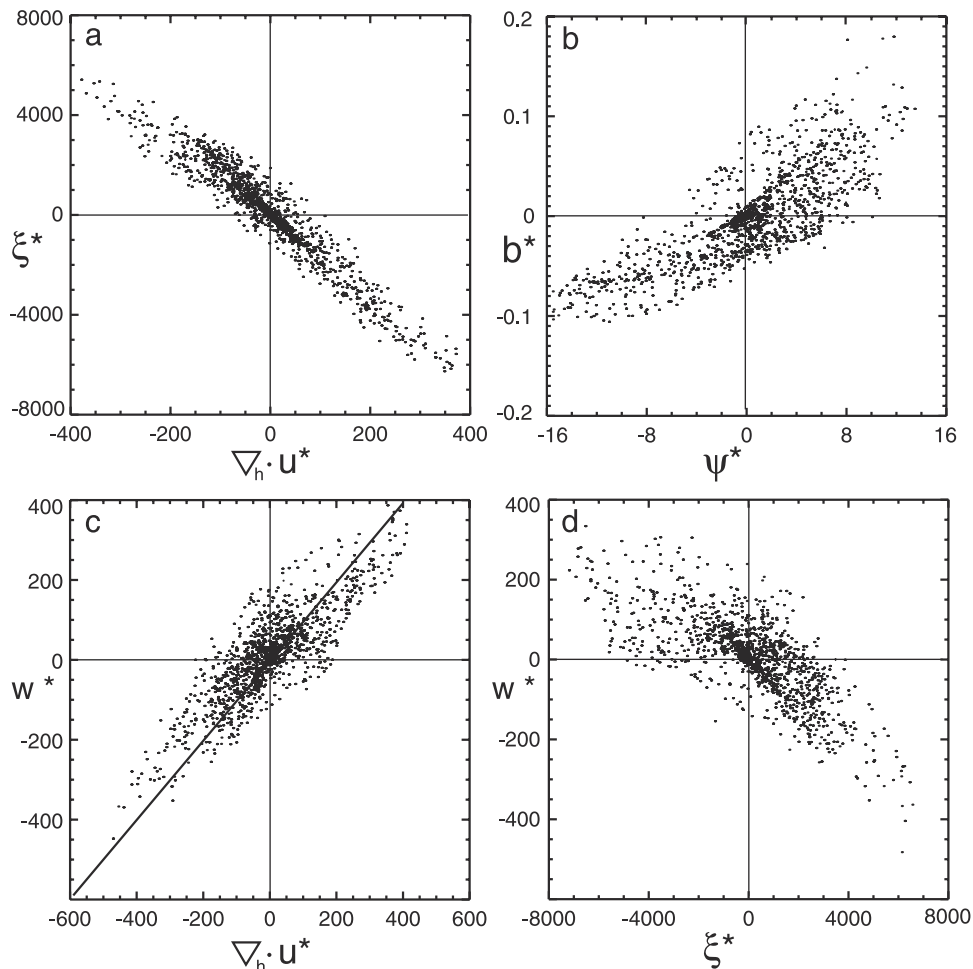
Figure 2. Scatter diagrams of the magnetic field and flow variables from the dynamo model shown in Figure 1. (a) Radial vorticity versus horizontal divergence at depth $z^* = 0.07$; (b) nonaxisymmetric part of the radial magnetic field at the outer boundary $z^* = 0$ versus toroidal stream function at depth $z^* = 0.07$; (c) diffusive magnetic image of upwelling versus horizontal divergence at $z^* = 0.07$; (d) diffusive magnetic image of upwelling versus radial vorticity at $z^* = 0.07$.

core surface flow, the part that is tangent to field intensity contours and induces no secular variation of its own. Using the dipole field amplitude and the magnetic diffusivity from the dynamo model, and assuming $c \simeq 2E^{-1/2}$ appropriate for Ekman pumping, equation (14) gives ψ^* (rms) $\simeq 3$ calculated from the nondipole field, versus ψ^* (rms) $\simeq 8$ from the actual numerical dynamo model. These values are consistent with the general behavior of this class of numerical dynamos: roughly one half of the upwelling in the columnar convection is attributable to Ekman pumping, with the remainder being due to buoyancy forces [*Olson et al.*, 1999].

[36] We have also calculated the correlation between the upwelling pattern and the other terms in the radial induction equation (1). We find that the global correlation between upwelling and the other terms in equation (1) is less than the correlation with the tangential diffusion, even though the magnitudes of some of these terms are far larger, in particular the secular variation and transport terms. An explanation we offer for this seemingly paradoxical finding is based on the concept of local equilibrium: the secular variation and transport terms in equation

(1) tend to nearly balance at leading order in the magnetic Reynolds number, and the upwelling and diffusion terms balance at the next order. Although these later terms do not form the primary balance, they are well correlated, since tangential diffusion tends to be large at the centers of upwellings and downwellings and small in the regions in between.

[37] The approach to local equilibrium depends somewhat on the structure of the convection, and may not occur in some dynamo models. Our tests were made using numerical dynamos that are dominated by narrow convection columns with smaller-scale, helical induction of the poloidal magnetic field. In these dynamos the radial field at the outer boundary is closely coupled to the pattern of convection. This relationship may be different for other dynamo types. In $\alpha\omega$-type dynamos for example, radial field concentrations at the outer boundary can be induced by outward diffusion of kinks in the strong toroidal component of the internal magnetic field. Indeed, we find that the agreement between the upwelling and the upwelling image is best for dynamo models without strong azimuthal flows. Conversely, the agreement tends to dimin-
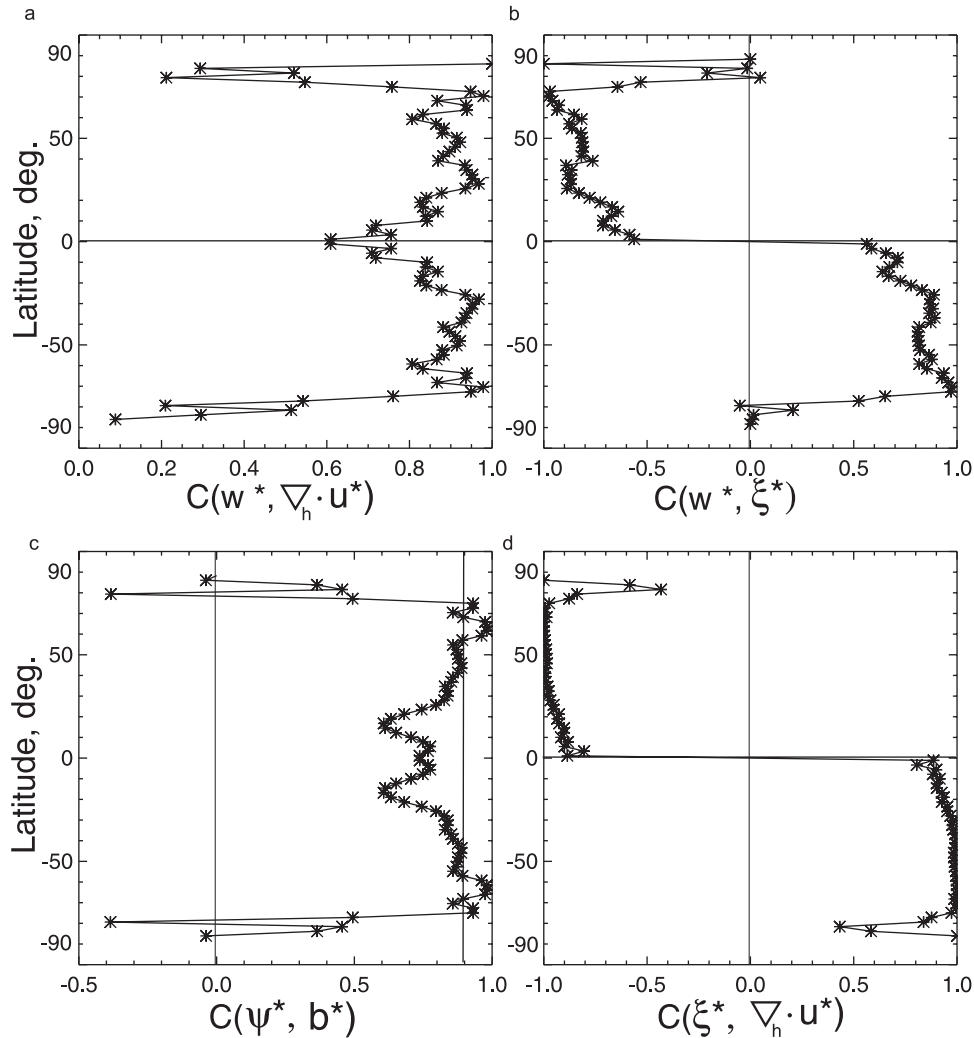
Figure 3. Correlation of magnetic field and flow variables as a function of latitude from the dynamo model shown in Figure 1. (a) Correlation between diffusive magnetic upwelling image and horizontal divergence at $z^* = 0.07$; (b) correlation between diffusive magnetic upwelling image and radial vorticity at $z^* = 0.07$; (c) correlation between toroidal stream function at $z^* = 0.07$ and nonaxisymmetric radial magnetic field at $z^* = 0$; (d) correlation between radial vorticity and horizontal divergence at $z^* = 0.07$.

ish as the strength of the azimuthal flow in the dynamo model increases.

4. Diffusive Flux Images of Upwellings From Geomagnetic Field Models

[38] We have applied this technique to instantaneous and time-averaged models of the geomagnetic field on the core-mantle boundary. Models of the core field representing four progressively longer time intervals are considered: (1) a snapshot at epoch 2000.0, the initial Oersted field model [*Olsen et al.*, 2000]; (2) a two decade average core field model derived by combining the Magsat field [*Cain et al.*, 1989] plus the initial Oersted field model; (3) a time average core field for 1900–2000 derived by combining Oersted, Magsat, plus the historic field model UFM1 of *Bloxham and Jackson* [1992]; and (4) a time average core field for 1700–2000 derived by combining the above core field models.

[39] Models of the core field derived from the Magsat and Oersted satellite measurements have nearly uniform global coverage and are typically truncated near spherical harmonic degree and order 14, due to the overlap with the crustal field [*Cain et al.*, 1989]. The historical field model UFM1 is also truncated at degree and order 14. Ground-based intensity data as well as directional data are used construct the historical core field models since about 1840, although the spatial coverage is not very uniform prior to about 1900. The earliest historical field models are based on directional information alone and are subject to limitations from sparse and nonuniform data coverage (see *Bloxham and Jackson* [1992] for details).

[40] Figure 4 shows the nondipole magnetic field on the core-mantle boundary from theses geomagnetic field models. The maps show the radial component of the magnetic induction in millitesla (mT) for the four time intervals with the axial dipole term removed, on a 5° × 5° grid. The maps are orthographic projections centered on the north pole, with
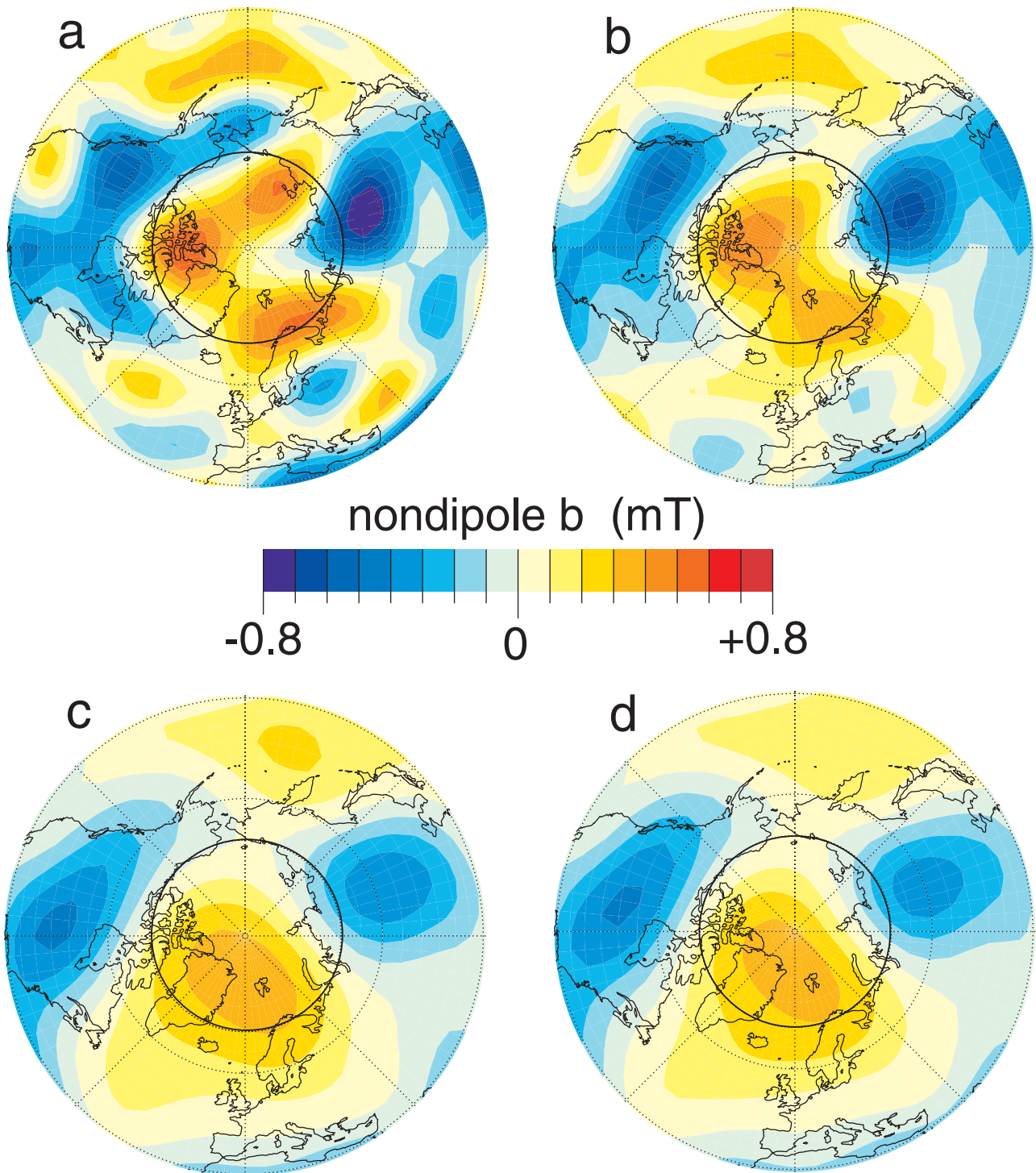
Figure 4. Nondipole part of the radial geomagnetic field on the core-mantle boundary. Northern hemisphere polar projections to 30°N latitude. The solid line indicates the inner core tangent cylinder intersection. (a) The 2000.0 initial Oersted field model; (b) time-average field model 1980–2000 from Magsat and Oersted; (c) time-average field model 1900–2000 from Magsat, Oersted and historical field model UFM1 of *Bloxham and Jackson* [1992]; (d) time-average field 1700–2000 from models in Figure 4c.

the continental outlines drawn for reference. The outer circle of each map is 30°N latitude, and the inner solid circle on each map is the cylindrical projection of the inner core onto the core-mantle boundary, the inner core tangent cylinder.

As seen in Figure 4, the basic structure of the time average nondipole field in the northern hemisphere consists of two patches with high magnetic flux density located beneath North America and Siberia, respectively, plus a low mag-
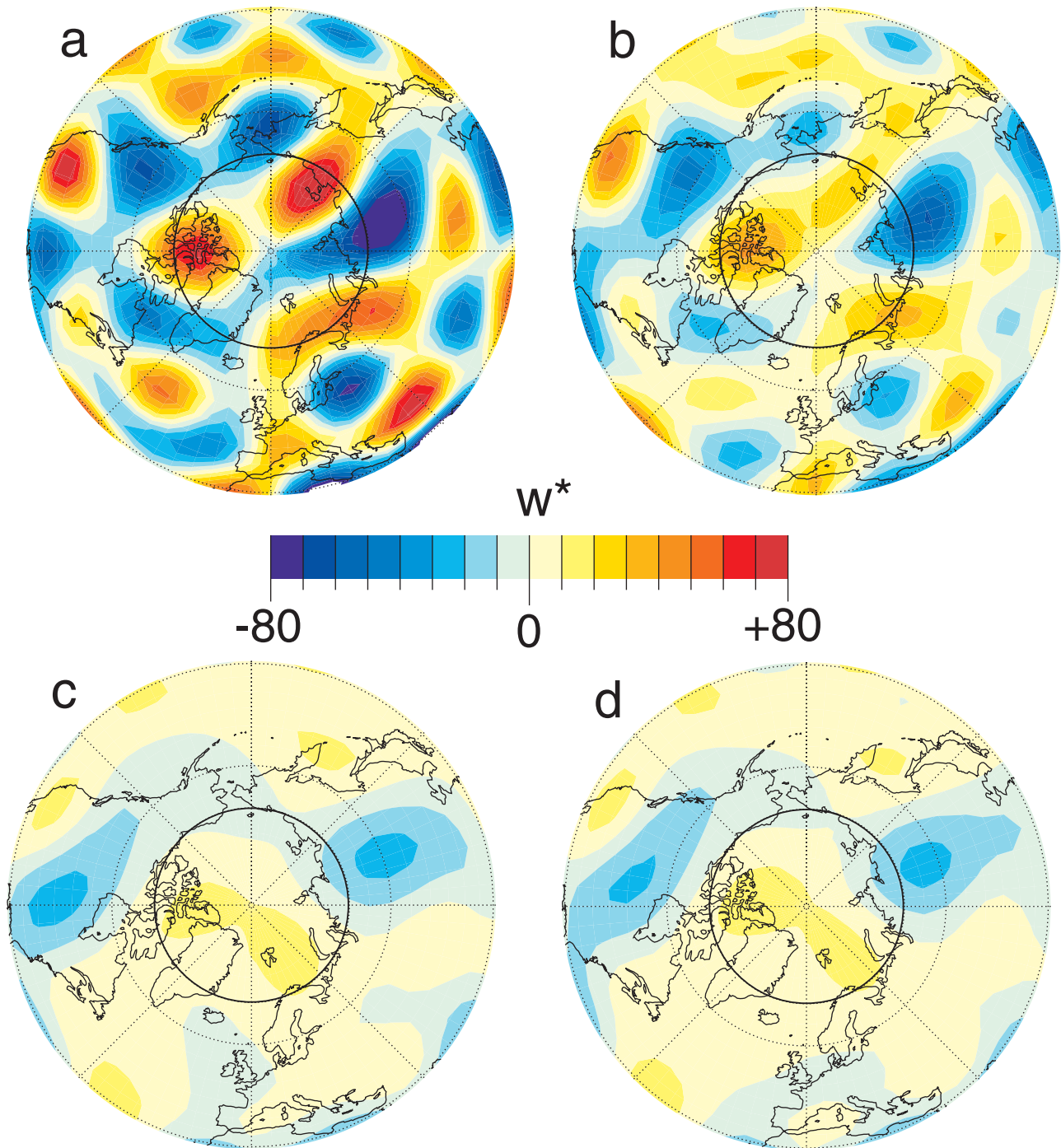
Figure 5. Diffusive magnetic upwelling images obtained from geomagnetic field models in Figure 4. (a) The 2000 snapshot; (b) 1980–2000 time average; (c) 1900–2000 time average; (d) 1700–2000 time average.

netic flux density patch beneath the north polar region. These structures are known to be present during much or all of the historical record [*Gubbins and Bloxham*, 1985]. In addition, northern hemisphere lobes with high magnetic flux density appear in some models of the time-averaged paleomagnetic field [*Kelly and Gubbins*, 1997; *Johnson and Constable*, 1997, 1998], but not in others [*Kono et al.*, 2000b]. In addition to the persistent longer-wavelength structures, there are shorter-wavelength structures, particu-

larly evident in the Oersted 2000 snapshot field model shown in Figure 4a. However, most of the short-wavelength features are transients that tend to average to zero in the longer time averages.

[41] Figure 5 shows the diffusive magnetic images of upwelling and downwelling pattern, derived from the non-dipole fields in Figure 4 using equation (10). The upwelling patterns are contoured in the dimensionless magnetic Reynolds number units defined in equation (16). Note the

difference in contour intervals used for the short-term averages in Figures 5a and 5b versus the longer-term averages in Figures 5c and 5d. As the averaging time increases, the shorter-wavelength features in the diffusive image are selectively removed, and a nearly stationary flow pattern emerges. The persistent structures in these images include fluid downwellings centered near the two high-density magnetic flux patches, and less well defined upwellings located between the upwellings. These persistent structures are not so evident in the image derived from the Oersted 2000 snapshot but are seen clearly in the images derived from time averages 20 years and longer, suggesting that the timescale for establishing local equilibrium in the core field is several decades. Although the upwelling pattern in the images is nearly stationary for longer time averages, there is a continual decrease in amplitude with increasing averaging time. The peak values of the upwelling magnetic Reynolds number steadily decrease from nearly 100 in the Oersted 2000 image (Figure 5a) to about 20 in the 300 year average image (Figure 5d).

[42] Assuming a linear relationship between the nondipole field and the toroidal stream function as in equation (14), the inferred circulation is counterclockwise around the two high-intensity flux patches and clockwise around the low-intensity flux regions separating them. That is, the inferred circulation is cyclonic where the flux intensity is high and anticyclonic where the flux intensity is low.

[43] The amplitude of the inferred cyclonic motion can be roughly estimated by assuming the downwellings are entirely due to turbulent Ekman pumping. Combining equations (14), (15), and (17) gives $c\Lambda^{-1/2}$ as the scale factor between the dimensionless toroidal stream function and the dimensionless nondipole field. Using a turbulent Ekman number $E = 10^{-8}$ (obtained by assigning the turbulent magnetic Prandtl equal one) we get $c = R/d \simeq E^{-1/2} \simeq 10^4$. According to this reasoning, the magnetic Reynolds number of the cyclonic toroidal flow inferred from the Oersted field model is of order 1000 and of order 500 in the 300 year time average. These are crude numbers at best, but they are broadly consistent with other estimates.

5.   Comparison With Other Upwelling Images

[44] Other images of the core upwelling pattern have already been constructed by applying the frozen flux technique to the historical geomagnetic field and its secular variation. Unfortunately, there is little consistency among these images, since the upwelling planforms inferred using frozen flux depend strongly on the closure assumption chosen, that is, on whether the flow is assumed to be tangentially geostrophic, steady, or toroidal.

[45]   For example, the assumption of tangential geostrophy,

$$\nabla_h \cdot (\mathbf{u}\cos\theta) = 0, \qquad (18)$$

when applied to the geomagnetic secular variation yields a pattern of alternating upwellings and downwellings concentrated near the equator [*Gire and Le Mouël*, 1990; *Bloxham and Jackson*, 1991]. Concentration of upwellings and downwellings near the equator in the tangentially geostrophic model is largely a consequence of the $(\tan\theta)^{-1}$

singularity in equation (18). Another closure constraint that has been used in conjunction with frozen flux is to assume the flow is steady over some finite interval of time [*Voorhies and Backus*, 1985]. When applied to the recent geomagnetic secular variation, the steady motions assumption yields a pattern of upwellings and downwellings that is strongest at middle latitudes, particularly in the regions beneath southern North America and southern Africa. A third closure constraint that is often used assumes the tangential velocity is purely toroidal, that is, fully represented by the stream function ψ in equation (16). Using this constraint together with frozen flux produces a pattern of horizontal velocity that is broadly similar to the tangential geostrophic constraint equation (18). However, the toroidal flow constraint together with frozen flux does not yield motions that are in anyway similar to diffusive flux. In the first place, purely toroidal flow implies zero radial motion and therefore zero upwellings [*Lloyd and Gubbins*, 1990; *Bloxham and Jackson*, 1991]. Second, the toroidal stream function obtained by frozen flux is orthogonal to ψ determined using equation (14).

6.   Discussion

[46] We have found that tangential magnetic diffusion correlates with fluid upwellings at the outer boundary in numerical dynamos where the primary flow is columnar-style convection. This relationship provides a simple technique for imaging the planform of the convection, using either snapshots or time averages of the radial magnetic field on the outer boundary of the conducting fluid. Comparison with dynamo model results shows that the diffusive magnetic image recovers the pattern and amplitude of the upwellings at high latitudes, particularly in the latitude band where the convection columns impinge on the outer core boundary. Conversely the diffusive image gives poor results at low magnetic latitudes (near the equator), where the assumptions underlying the method break down.

[47] Diffusive magnetic images derived from models of the historical geomagnetic field at the core-mantle boundary representing four different time averages show a consistent image in the northern hemisphere. The persistent, high-intensity magnetic flux patches arrayed around the inner core tangent cylinder correspond to fluid downwellings in the diffusive magnetic image, with an inferred anticyclonic circulation around them. In between the high-flux regions, the diffusive image shows fluid upwellings with an inferred cyclonic circulation.

[48] *Gubbins and Bloxham* [1987] have already interpreted the two high-latitude magnetic flux bundles in the northern hemisphere in terms of columnar-style convection with axial downwellings. They proposed that the location of the flux patches, just outside of the inner core tangent cylinder, indicates a topographic control by the solid inner core on columnar convection in the fluid outer core. Our diffusive magnetic images from time averaged geomagnetic field models support this interpretation.

[49] An interesting question is whether the diffusive magnetic images in Figure 5 represent the primary scale of convection in the core, or alternatively, represent a residual, spatial average of convective motions occurring on smaller scales. The decrease we infer in upwelling

velocity with increasing long time average seems to favor the second possibility.

References

Backus, G., Kinematics of geomagnetic secular variation in a perfectly conducting core, *Philos. Trans. R. Soc. London, Ser. A*, *263*, 239–266, 1968.

Bloxham, J., Simple models of fluid flow at the core surface, *Geophys. J. Int.*, *99*, 173–182, 1989.

Bloxham, J., and A. Jackson, Fluid flow near the surface of Earth's outer core, *Rev. Geophys.*, *29*, 97–120, 1991.

Bloxham, J., and A. Jackson, Time dependent mapping of the geomagnetic field at the core-mantle boundary, *J. Geophys. Res.*, *97*, 19,357–19,564, 1992.

Bullard, E. C., C. Freedman, H. Gellman, and J. Nixon, The westward drift of the Earth's magnetic field, *Philos. Trans. R. Soc. London, Ser. A*, *243*, 67–92, 1950.

Cain, J. C., Z. Wang, C. Kluth, and D. R. Schmitz, Derivation of a geomagnetic field model to $n = 63$, *Geophys. J. Int.*, *97*, 431–441, 1989.

Christensen, U., P. Olson, and G. A. Glatzmaier, Numerical modeling of the geodynamo: A systematic parameter study, *Geophys. J. Int.*, *138*, 393–409, 1999.

Elsasser, W. M., Induction effects in terrestrial magnetism, part III, Electric modes, *Phys. Rev.*, *72*, 821–833, 1947.

Gire, C., and J. L. Le Mouël, Tangentially geostrophic flow at the core-mantle boundary compatible with the observed geomagnetic secular variation: the large-scale component of the flow, *Phys. Earth Planet. Inter.*, *59*, 259–287, 1990.

Glatzmaier, G. A., and P. H. Roberts, Rotation and magnetism of Earth's inner core, *Science*, *274*, 1887–1891, 1996.

Greenspan, H., *The Theory of Rotating Fluids*, 400 pp., Cambridge Univ. Press, New York, 1968.

Gubbins, D., A formalism for the inversion of geomagnetic data for core motions with diffusion, *Phys. Earth Planet Inter.*, *98*, 193–206, 1996a.

Gubbins, D., A difficulty with using the frozen flux hypothesis to find steady core motions, *Geophys. Res. Lett.*, *23*, 1825–1828, 1996b.

Gubbins, D., and J. Bloxham, Morphology of the geomagnetic field and implications for the geodynamo, *Nature*, *325*, 509–511, 1987.

Gubbins, D., and P. H. Roberts, Magnetohydrodynamics of the Earth's core, in *Geomagnetism*, vol. 2, edited by J. A. Jacobs, pp. 1–183, Academic, San Diego, Calif., 1987.

Halley, E., An account of the cause of change of the variation of the magnetic needle, with an hypothesis of the structure of the internal parts of the Earth, *Philos. Trans. R. Soc. London, Ser. A*, *16*, 563–578, 1692.

Johnson, C. L., and C. G. Constable, The time averaged geomagnetic field: global and regional biases for 0–5 Ma, *Geophys. J. Int.*, *131*, 643–666, 1997.

Johnson, C. L., and C. G. Constable, Persistently anomalous Pacific geomagnetic fields, *Geophys. Res. Lett*, *25*, 1011–1014, 1998.

Kelly, P., and D. Gubbins, The geomagnetic field over the past 5 million years, *Geophys. J. Int.*, *128*, 315–330, 1997.

Kageyama, A., and T. Sato, Generation mechanism of a dipole field by a magnetohydrodynamical dynamo, *Phys. Rev. E*, *55*, 4617–4626, 1997.

Kono, M., A. Sakuraba, and M. Ishida, Dynamo simulation and paleosecular variation models, *Philos. Trans. R. Soc. London, Ser. A*, *358*, 1123–1139, 2000a.

Kono, M., H. Tanaka, and H. Tsunakawa, Spherical harmonic analysis of paleomagnetic data: The case of linear mapping, *J. Geophys. Res.*, *105*, 5817–5833, 2000b.

Kuang, W., and J. Bloxham, An Earth-like numerical dynamo model, *Nature*, *389*, 371–374, 1997.

Lloyd, D., and D. Gubbins, Toroidal fluid motion at the top of Earth's core, *Geophys. J. Int.*, *100*, 455–467, 1990.

Love, J. J., A critique of frozen-flux inverse modelling of a nearly steady geodynamo, *Geophys. J. Int.*, *138*, 353–365, 1999.

Moffatt, H.K., *Magnetic Field Generation in Electrically Conducting Fluids*, 343 pp., Cambridge Univ. Press, New York, 1978.

Olsen, N., et al., initial field model, Geophys, Res. Lett., *27*, 3607–3611, 2000.

Olson, P., and G. A. Glatzmaier, Magnetoconvection and thermal coupling of the Earth's core and mantle, *Philos. Trans. R. Soc. London, Ser. A*, *354*, 1413–1424, 1996.

Olson, P., U. Christensen, and G. A. Glatzmaier, Numerical modeling of the geodynamo: Mechanisms of field generation and equilibration, *J. Geophys. Res.*, *104*, 10,383–10,404, 1999.

Rau, S., U. Christensen, A. Jackson, and J. Wicht, Core flow inversion tested with numerical dynamo models, *Geophys. J. Int.*, *141*, 485–497, 2000.

Roberts, P. H., and G. A. Glatzmaier, A test of the frozen-flux approximation using a new geodynamo model, *Philos. Trans. R. Soc. London, Ser. A*, *358*, 1109–1121, 2000.

Roberts, P. H., and D. Gubbins, Origin of the main field: Kinematics, in *Geomagnetism*, vol. 2, edited by J. A. Jacobs, pp. 184–249, Academic, San Diego, Calif., 1987.

Roberts, P. H., and S. Scott, On analysis of secular variation, 1, A hydromagnetic constraint, *J. Geomagn. Geoelectr.*, *17*, 137–151, 1965.

Voorhies, C. V., Steady flows at the top of Earth's core derived from geomagnetic field models, *J. Geophys. Res.*, *91*, 12,444–12,466, 1986.

Voorhies, C. V., Time-varying flows at the top of Earth's core derived from definitive geomagnetic reference models, *J. Geophys. Res.*, *100*, 10,029–10,039, 1995.

Voorhies, C. V., and G. E. Backus, Steady flows at the top of the core from geomagnetic field models: The steady motions theorem, *Geophys. Astrophys. Fluid Dyn.*, *32*, 163–173, 1985.

Whaler, K. A., Geomagnetic evidence for fluid upwelling at the core-mantle boundary, *Geophys. J. R. Astron. Soc.*, *86*, 563–588, 1986.

———————————

J. Aurnou, Department of Terrestrial Magnetism, Carnegie Institution of Washington, Washington, DC 20015, USA. (jona@dtm.ciw.edu)

P. Olson, Department of Earth and Planetary Sciences, Johns Hopkins University, Baltimore, MD 21218, USA. (olson@jhu.edu)

I. Sumita, Department of Earth Sciences, Faculty of Science, Kanazawa, 920-1192, Japan. (sumita@hakusan.s.kanazawa-u.ac.jp)